Editors' Suggestion

Inverse Design of an Ultrasparse Dissipated-Sound Metacage by Using a Genetic Algorithm

Houyou Long,[1] Yuanzhou Zhu,[1] Ye Gu,[1] Ying Cheng,[1,2,*] and Xiaojun Liu[1,2,†]

[1] *Department of Physics, MOE Key Laboratory of Modern Acoustics, Collaborative Innovation Center of Advanced Microstructures, Nanjing University, Nanjing 210093, China*

[2] *State Key Laboratory of Acoustics, Institute of Acoustics, Chinese Academy of Sciences, Beijing 100190, China*

(Received 2 June 2022; accepted 1 September 2022; published 13 October 2022)

Acoustic metasurfaces have the potential to be a promising route for the development of compact sound-absorptive devices with ventilation capability. However, the dissipation mechanism of limited plane wave fronts and elaborate geometry configured by extensive parametric sweepings severely restricts the available designs. Here, via establishing a cylindrical transfer matrix method combined with an inverse-design strategy of a genetic algorithm, we construct an optimized ultrasparse (with filling ratio of framework at 50%) dissipated-sound metacage (DSM), which theoretically (experimentally) demonstrates 99.1% (98.2%) absorptance for omnidirectionally radiated cylindrical sound at a prescribed frequency of 260 Hz in deep-subwavelength thickness. The perfect absorption is ascribed to the mode hybridization between two resonant meta-atoms in which one acts as a dissipated mode and the other as an acoustically soft boundary. Moreover, the balance between thickness and sparsity is investigated by demonstrating DSMs that show different filling ratios of air channels. We finally extend the paradigm into a broadband regime for exploring more potential practicability.

DOI: 10.1103/PhysRevApplied.18.044032

I. INTRODUCTION

The ever-growing area of acoustic metamaterials and metasurfaces has empowered the design of devices that can manipulate sound in a desired and prescribed manner by rationally decorating subwavelength structures [1,2]. Numerous acoustic metadevices enabling unconventional phenomena such as sound superlensing [3,4], acoustic holography [5,6], acoustic cloaking [7–9], undisturbed sound transmission [10,11], to name a few, are developed. Recently, a common type of metasurface [12–21] has been designed as a low-frequency sound sink, which demonstrates superiority to a conventional porous-materials-based sound absorber relying on linear response theory [22]. Via coupling multiple detuned resonant meta-atoms, the absorbers showing broadband high-efficiency absorptions can be realized [23–28]. Moreover, it has been shown that effective hybridization between two or more resonant meta-atoms in a dual-port system are demanded to build a multifunctional absorber, namely, not merely with high efficiency but also with asymmetric absorption, excellent ventilation, and heat-conduction performances [29–36]. To date, several mechanisms including hybridizing detuned (tuned) modes under the same (different) damped states [30–33], coupling resonant modes, and a nonresonant reactance-dominated boundary [37] have been proposed to construct ventilated absorbers. The designed absorber can present promising absorption and ventilation performances by carefully decorating geometric parameters.

However, the above-mentioned absorbers are designed for suppressing, normally or obliquely (at a specific angle), an incident plane wave but do not involve omnidirectionally radiated cylindrical sound. In the context of cylindrical sound waves, an acoustical metacage that can shield sound has been proposed [38,39]. However, sound energy is only localized inside the structure but not dissipated. To date, a ventilated absorber for cylindrical sound wave has not been developed. In addition, the geometry of the above-mentioned metadevices [30–35,37–39] are fine tuned by iteratively performing full-wave numerical simulations. The trial-and-error method largely relies on human experience gained from physical intuition, which is largely time consuming, let alone for limited parameters being searched.

Recently, based on iterative optimization of a figure of merit, inverse-design approaches capable of discovering final devices with free-from layouts and nonintuitive characteristics, have been rapidly developed to design devices outperforming empirically designed structures in various wave fields [40–42]. In this work, a paradigm to realize an ultrasparse dissipated sound metacage (DSM) that can

*chengying@nju.edu.cn
†liuxiaojun@nju.edu.cn

perfectly absorb the enclosed cylindrical sound wave is proposed via hybridizing multiple resonant meta-atoms with geometrical parameters optimized by an inverse-design strategy of a genetic algorithm (GA). A GA is a gradient-free optimization algorithm mimicking a biological evolution process, including selection, crossover, and mutation operators [43–46], in which a candidate population is characterized by a chromosome comprising structure parameters to be optimized and the fitness function is determined by the desired response produced by the structure. Thus, a selection process can be conducted by the ranked fitness functions to select the most promising chromosomes for producing next generations. Crossover and mutation operators are then used to generate children. Hence, an alternative population is generated, which suggests an iteration is done. A transfer matrix method for cylindrical wave (CTMM) is developed to acoustically characterize the DSM and operate a GA for achieving the optimal configurations. The demonstrated ultrasparse (filling ratio of framework at 50%) DSM present 99.1% (98.9%) absorption in CTMM (finite-element method, FEM) for cylindrical sound at 260 Hz, which is validated by experimental measurement conducted in a fan-shaped impedance tube. The high-efficiency absorption arises from the efficient coupling between two constitutive resonators in which one plays a dissipated meta-atom and the other an acoustically soft boundary. Moreover, it is demonstrated that the structure goes deeper-subwavelength by decreasing the filling ratio of air channels. Further, we extend the methodology into the broadband regime. As a demonstration, we construct a DSM showing $> 80\%$ absorption from 257 to 289 Hz in which > 10 dB sound transmission loss is obtained.

II. THEORETICAL MODEL

Sketched in Figs. 1(a) and 1(b) are the three-dimensional (3D) stereogram and two-dimensional (2D) top view of the proposed ultrasparse DSM, which is circularly arrayed by a metamolecule composed of two folded Fabry-Perot resonators (FPRs) [inset of Fig. 1(b)]. Each metamolecule occupies an angle of α in azimuthal direction therein β is for the angle of air channel between adjacent meta-atoms. Thus, the filling ratio of air channel follows $\eta = \beta/\alpha$. The inner and outer radius of the metacage are R_1 and R_2, respectively. The width of the folded channel for the ith FPR ($i = 1, 2$) is w_i, as presented in the inset where l_1, l_t and l_2 are correspondingly for the distances between FPR1 to the inner boundary, FPR1 to FPR2, and FPR2 to the outer boundary. The DSM aims to consume sound waves radiated from the line source located at its center, indicating that both the reflected and transmitted sound are suppressed (no reflected wave back to region I while no transmitted wave into region II), as schemed in Fig. 1(b). Here, we set $\alpha = 20^\circ$ and $\beta = 10^\circ$, leading to an ultrasparse DSM ($\eta = 50\%$) to guarantee excellent ventilation performance.

In order to provide physical description on the proposed DSM, CTMM that relates the sound pressure and velocity in regions I and II is developed as

$$\begin{bmatrix} p^{\mathrm{I}} \\ S_1 v^{\mathrm{I}} \end{bmatrix} = \mathbf{T} \begin{bmatrix} p^{\mathrm{II}} \\ S_2 v^{\mathrm{II}} \end{bmatrix} = \begin{bmatrix} T_{11} & T_{12} \\ T_{21} & T_{22} \end{bmatrix} \begin{bmatrix} p^{\mathrm{II}} \\ S_2 v^{\mathrm{II}} \end{bmatrix}, \quad (1)$$

where $\mathbf{T} = \mathbf{T}_{t1}\mathbf{T}_{\mathrm{FPR1}}\mathbf{T}_{t2}\mathbf{T}_{\mathrm{FPR2}}\mathbf{T}_{t3}$ with $\mathbf{T}_{t1}$, $\mathbf{T}_{t2}$ and $\mathbf{T}_{t3}$ being the transfer matrices relating the inner boundary to FPR1, FPR1 to FPR2, and FPR2 to the outer boundary, respectively [47]; $\mathbf{T}_{\mathrm{FPR}i} = \begin{bmatrix} 1 & 0 \\ 1/Z_{\mathrm{FPR}i} & 1 \end{bmatrix}$ ($i = 1, 2$) denotes for the transfer matrix of ith FPR with $Z_{\mathrm{FPR}i}$ being the impedance of FPRi. Sound pressure and radical velocity in each region are derived by solving the wave equation in the cylindrical coordinates, which are

$$p^{\mathrm{I}} = X_1 H_0^{(1)}(k_0 r) + Y_1 H_0^{(2)}(k_0 r), \quad (2a)$$

$$v^{\mathrm{I}} = -\frac{1}{jZ_0}\left(X_1 H_0^{'(1)}(k_0 r) + Y_1 H_0^{'(2)}(k_0 r)\right), \quad (2b)$$

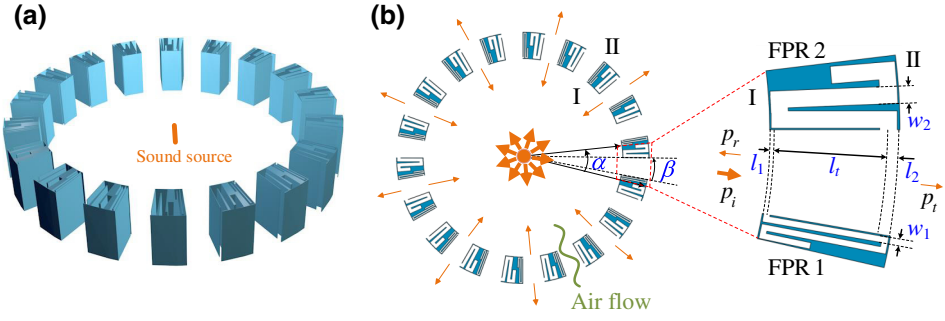

FIG. 1. (a) 3D and (b) 2D view of the proposed ultrasparse DSM. Inset of (b): a metamolecule composed of two FPRs termed as FPR1 and FPR2.

and

$$p^{\mathrm{II}} = Y_2 H_0^{(2)}(k_0 r), \tag{3a}$$

$$v^{\mathrm{II}} = -\frac{1}{jZ_0} Y_2 H_0^{'(2)}(k_0 r), \tag{3b}$$

where $H_0^{(1)}$ and $H_0^{(2)}$ correspond to the zero-order Hankel function of the first kind denoting converging waves and the second kind diverging waves; $H_0^{'(1)}$ and $H_0^{'(2)}$ are the corresponding derivative with respect to r; $j = \sqrt{-1}$ denotes the imaginary unit; k_0 and Z_0 are the wave number and sound impedance of background medium. By substituting Eqs. (2) and (3) into Eq. (1), the reflection coefficient r_p and transmission coefficient t_p of sound pressure are derived as

$$r_p = \frac{X_1}{Y_1} = \frac{V H_0^{'(2)}(k_0 R_1) - H_0^{(2)}(k_0 R_1)}{H_0^{(1)}(k_0 R_1) - V H_0^{'(1)}(k_0 R_1)}, \tag{4a}$$

$$t_p = \frac{Y_2}{Y_1} = \frac{r H_0^{(1)}(k_0 R_1) + H_0^{(2)}(k_0 R_1)}{T_{11} H_0^{(2)}(k_0 R_2) + \frac{jS_2}{Z_0} T_{12} H_0^{'(2)}(k_0 R_2)}, \tag{4b}$$

where the coefficient V follows

$$V = \frac{T_{11} H_0^{(2)}(k_0 R_2) + \frac{jS_2}{Z_0} T_{12} H_0^{'(2)}(k_0 R_2)}{\frac{Z_0}{jS_1} T_{21} H_0^{(2)}(k_0 R_2) + \frac{S_3}{S_1} T_{22} H_0^{'(2)}(k_0 R_2)}. \tag{5}$$

$S_1 = R_1 H$ and $S_2 = R_2 H$ are the edge areas of regions I and II, respectively. Thus, via substituting Eq. (2), the sound intensity $I = 1/2\,\mathrm{Re}\{p\,v^*\}$ for incident wave at $r = R_1$ can be given as

$$\begin{aligned} I_i &= \frac{1}{2}\mathrm{Re}\left\{ Y_1 \left[J_0(k_0 R_1) - jN_0(k_0 R_1)\right] \left(\frac{jY_1}{2Z_0} \left[J_{-1}(k_0 R_1) \right.\right.\right. \\ &\quad \left.\left.\left. - jN_{-1}(k_0 R_1) - J_1(k_0 R_1) + jN_1(k_0 R_1)\right] \right)^* \right\} \\ &= \frac{Y_1^2}{2Z_0} \left\{ J_0(k_0 R_1) N_0^{'}(k_0 R_1) - N_0(k_0 R_1) J_0^{'}(k_0 R_1) \right\}. \end{aligned} \tag{6}$$

Similarly, the sound intensities for reflected and transmitted waves can be derived as

$$I_r = \frac{X_1^2}{2Z_0} \left\{ N_0(k_0 R_1) J_0^{'}(k_0 R_1) - J_0(k_0 R_1) N_0^{'}(k_0 R_1) \right\}, \tag{7a}$$

$$I_t = \frac{Y_2^2}{2Z_0} \left\{ J_0(k_0 R_2) N_0^{'}(k_0 R_2) - N_0(k_0 R_2) J_0^{'}(k_0 R_2) \right\}, \tag{7b}$$

where $J_0(k_0 r)$ and $N_0(k_0 r)$ are the zero-order Bessel and Neumann functions, which satisfy the relationships $H_0^{(1)}(k_0 r) = J_0(k_0 r) + jN_0(k_0 r)$ and $H_0^{(2)}(k_0 r) = J_0(k_0 r) - jN_0(k_0 r)$. Thus, corresponding coefficients for sound energy can be obtained as

$$R = \frac{I_r S_1}{I_i S_1} = \left| \frac{X_1^2}{Y_1^2} \right|, \quad T = \frac{I_t S_2}{I_i S_1} = \left| \frac{Y_2^2}{Y_1^2} \right|. \tag{8}$$

The absorption coefficient is given by $A = 1 - R - T$.

III. RESULTS AND DISCUSSION

A. Optimization by GA

It is demonstrated that the channel width and length of a FPR are vital to decorate its externally observable dissipated loss, radiated loss, and resonant frequency [26]. Specifically, w_1 and w_2 determine the loss and radiation of FPR1 and FPR2; l_{c1} and l_{c2} influence the corresponding resonant frequencies; l_t characterizes the coupling intensity between two adjacent FPRs. Hence, it necessitates to cautiously decorate these geometric parameters to maximize the absorption at a prescribed frequency, i.e., 260 Hz in this work for illustration, which is cumbersome in traditional parametric-sweeping manner even with the guidance of empirical knowledge. Factually, it is typically an inverse-design problem, which aims to determine the optimal structure from the targeted sound response. Hence, we here adopt GA, a metaheuristic inspired by the rule of natural selection, to optimize geometric configurations [43,48]. As a type of evolutionary algorithm, GA can capture global optima by using bioinspired operators containing selection, crossover, and mutation, in which many strategies maintaining the randomness and diversity in a population may overcome the local optimum trap of a gradient-based algorithm such as topology optimization [49] and an adjoint variable algorithm [50,51]. Moreover, unlike a data-driven deep-learning algorithm [52], evolutionary-based GA does not need to produce a gigantic amount of well-labeled datasets. Additionally, due to its gradient-free methodology, GA can address problems with discrete parameters [43,48].

The optimization process is illustrated in Fig. 2(a). GA starts from randomly generating the initial population (the total number of population is 6000 here), and each candidate solution is regarded as a chromosome coded by binary-value (0 and 1) gene. Each gene contains the values of physical parameters to be optimized (including w_1, w_2, l_1, l_2, and l_t). Then, a fitness function is defined as the absorptance at prescribed frequency, and the fitness value of each candidate can be evaluated. Thus, we can rank the more excellent chromosomes according to the fitness values from largest to smallest. This step aims to regulate the gene library for conducting subsequent selection operation. Here, a roulette wheel method is employed to select promising chromosomes as the parents for producing next generations. Then, the one-point crossover

operator (crossover rate at 0.6) is employed to produce the children generations containing the chromosome from parents and the mutation operator (mutation rate at 0.01) to produce alternative genes that are not presented in the original population. Finally, an alternative population is produced and the fitness can be evaluated, which mathematically maps an iteration process being done. The next iteration will be continued if the result is not convergence otherwise terminated.

For visualizing the evolutionary process, we here distribute two genes (w_1 and w_2) of therein 300 candidate solutions at the 1st, 100th, and 600th iteration, as shown in Fig. 2(b). Initially, the algorithm has no knowledge about the design space and the populations are randomly spanning the full specific range. Over the course of iteration, the distribution of population gets narrow and converges to the best solution ultimately (the total iteration number here is 600), which can be confirmed by the narrowing gap between the mean and max fitness as presented in Fig. 2(c). Here, the mean fitness is averaged by the fitness of all the solutions, whereas the max fitness stands for the best solution in current populations. After enough iterations, the mean fitness equals to the max one and the iteration process is terminated. The optimized geometric parameters are listed in Table I.

TABLE I. Geometric parameters of FPRs (unit, mm).

w_1	w_2	l_1	l_2	l_t	R_1	R_2
6.6	17.9	318.8	325.9	115	498.5	631.5

B. Absorption performance and physical mechanism

We here proceed to characterize the DSM with optimized geometrical parameters listed in Table I. The scattering spectra are presented in Fig. 3(a), where the aqua dashed line (triangles), gray dash dotted line (squares), and wine solid line (circles) show the reflectance, transmittance, and absorptance calculated by CTMM (FEM). Here, FEM is conducted by pressure acoustic, frequency modulus in COMSOL Multiphysics. Complex parameters including mass density and bulk modulus given by Stinson's model are employed to characterize the viscous and heat dissipation of FPRs [53]. The scattering coefficients in FEM are calculated by retrieving the sound pressures at three radial positions (see Appendix A). It is observed from Fig. 3(a) that near-zero reflectance and transmittance are achieved at 260 Hz, suggesting that the sound waves radiated from the center line source can neither be reflected by nor transmitted through the DSM. Therefore, instead of merely localizing sound energy inside the structure in previous works [38,39], the DSM here can almost totally consume the incident sound energy since the absorptance of 99.1% in CTMM and 98.9% are achieved.

Figure 3(b) presents the distributions of absolute sound pressure $|p|$ (upper panel) and total power dissipation density Q_p (lower panel) at 260 Hz. Note that the radiated sound energy is concentrated in FPR1. Due to the high energy density, the sound wave is dominantly dissipated by FPR1 via viscous friction between air particle and FPR1 framework, as illustrated by the Q_p distribution. On the other hand, FPR2 plays the role of an acoustically soft

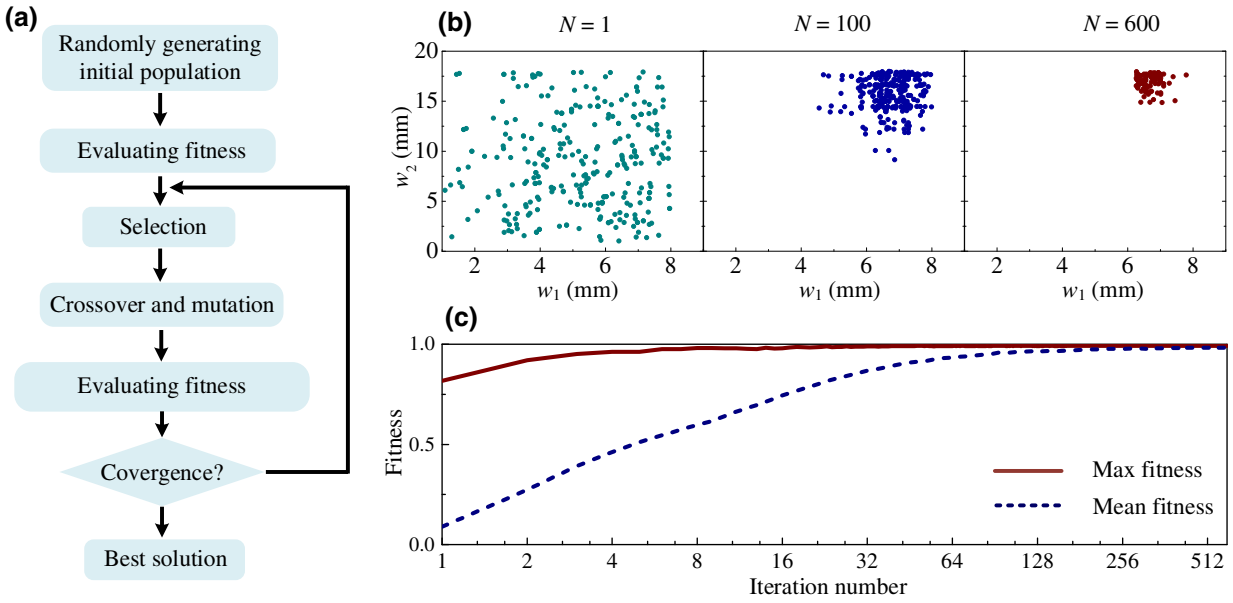

FIG. 2. (a) Flow graph of the genetic algorithm. (b) Distributions of w_1 and w_2 in iteration number at 1, 100, and 600. (c) Mean (dashed line) and max fitness (solid line) in iterative progress.

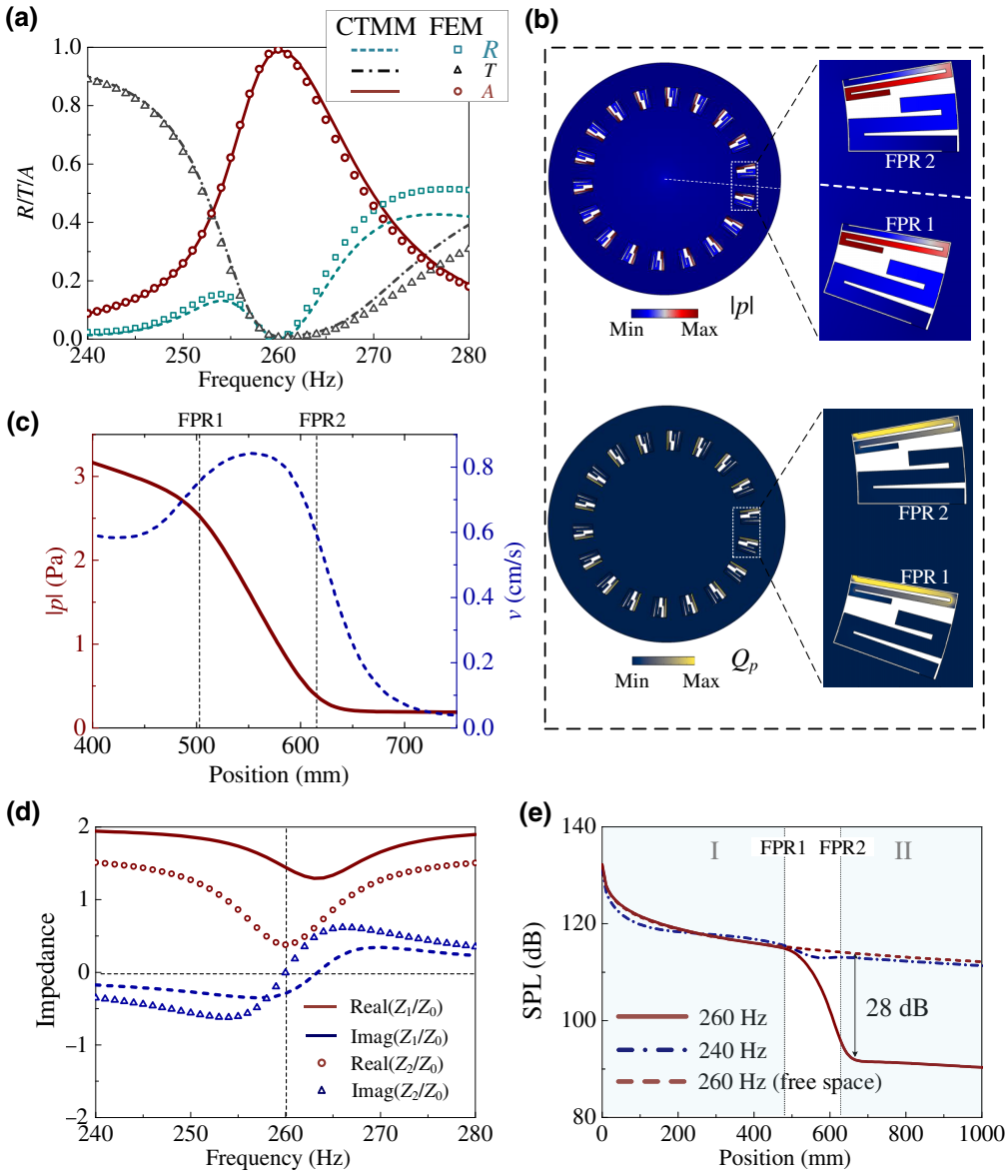

FIG. 3. (a) Reflectance (dashed line, squares), transmittance (dash-dotted line, triangles), and absorptance (solid line, circles) of the DSM derived from CTMM and FEM. (b) Absolute sound pressure $|p|$ and total power dissipation density Q_p distribution at 260 Hz. (c) Absolute sound pressure (solid line) and velocity (dashed line) distribution along the radial channel [white dashed line in (b)]. (d) Normalized impedance of FPR1 and FPR2. (e) SPL distribution along the radius.

boundary presenting the sound-pressure node and velocity antinode [30,35], as confirmed by the distributes of $|p|$ and v in Fig. 3(c) along the white dashed lines [see inset in Fig. 3(b)]. Quantitatively, the sound impedance of FPR1 (lines) and FPR2 (symbols) are presented in Fig. 3(d). Their corresponding relative sound impedances normalized by air are $1.44 - 0.29j$ and $0.38 - 0.007j$ at 260 Hz, confirming the acoustically soft boundary characteristics of FPR2. Thus, the sound waves encountered to FPR2 will be reflected and then trapped by FPR1 to produce high-performance absorptions.

Additionally, we depict the profiles of sound-pressure level (SPL) along the radius in Fig. 3(e), which demonstrate that SPL at 260 Hz is rapidly attenuated inside the DSM region, which leads to approximately 28-dB drops compared with that in free space (without DSM). Moreover, the coincidence between SPL with and without DSM in region I suggests that sound is hardly reflected. For reference, SPL at 240 Hz is illustrated in Fig. 3(e), which demonstrates that the sound energy at the frequency can hardly be shielded by the structure. We emphasize that in addition to the ultrasparsity, the DSM is in subwavelength

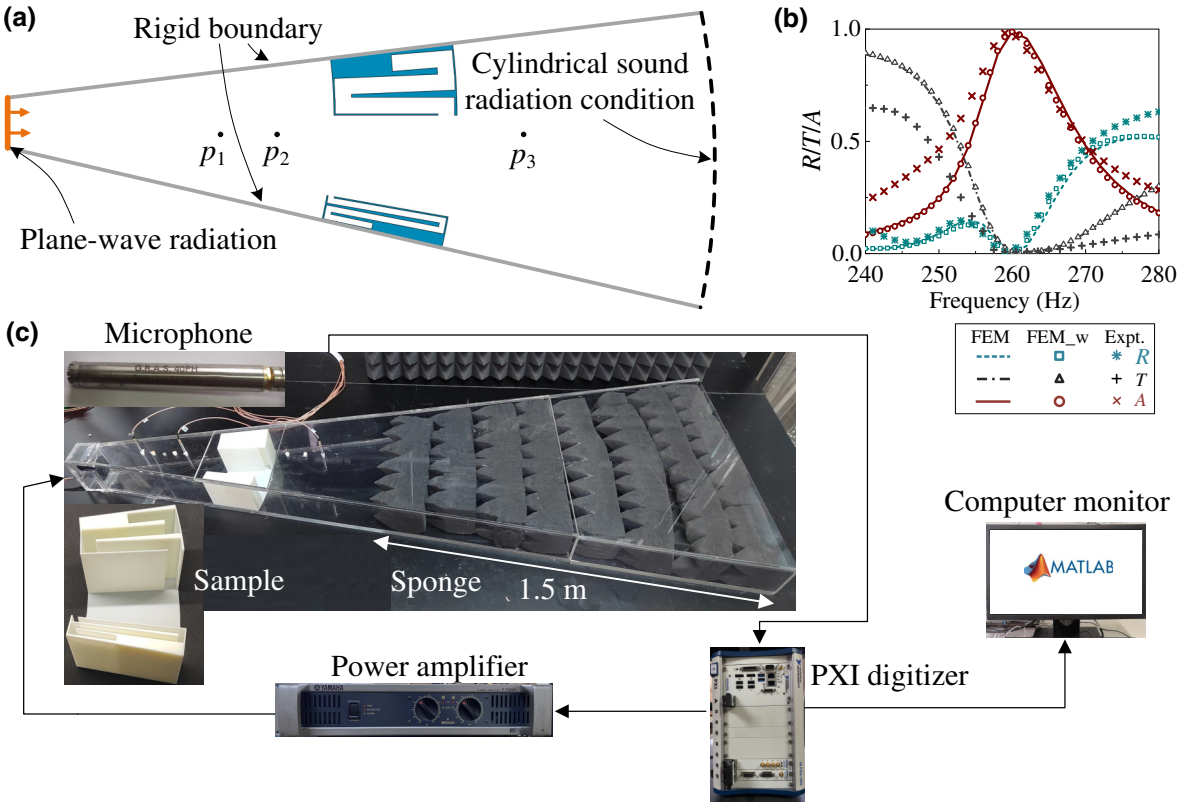

FIG. 4. (a) 2D schematics of the conceptual experiment, where p_1, p_2, and p_3 are test points to retrieve sound pressures. (b) Acoustic spectra derived from the annular structure (lines), the metamolecule in waveguide (open symbols) calculated by FEM and experimental measurement (solid symbols). (c) Photograph of the experimental setup.

scale as the thickness of 133 mm is approximately $1/10\lambda$ (λ being the wavelength at 260 Hz).

C. Experimental demonstration

In this subsection, experimental proof of the designed DSM is presented. Considering the intense scattering characteristics of sound low to 260 Hz, we here conduct experimental measurement in a fan-shaped impedance tube for simplicity. The effectiveness of the measuring method is firstly proven by a conceptual experiment conducted in numerical simulation software, as sketched in Fig. 4(a). In simulations, the acoustically rigid boundary is set on both lateral sides; plane sound wave is excited from the left side to simulate a line sound source due to the much larger wavelength (1.32 m) than the dimension of sound source (length at 0.03 m); cylindrical wave radiation condition is applied at the output terminal. The scattering coefficients are achieved by substituting the retrieved sound pressures at points p_1, p_2, and p_3 into Eqs. (A3) and (8). Acoustic spectra derived from the annular structure and the metamolecule in the waveguide are presented by lines and open symbols in Fig. 4(b), which show excellent consistence confirming the effectiveness of the proposed measurement method in the impedance tube.

Physical experimental setup is depicted in Fig. 4(c). The DSM sample fabricated by epoxy resin is sandwiched inside the 2D plexiglass waveguide with wall thickness of 10 mm. Cone-shaped sound porous materials with a length of 1.5 m is placed at the terminal to function as an anechoic boundary. In experiments, the input signals are generated by an arbitrary waveform generator (NI PXI-5421) and amplified by an audio power amplifier (YAMAHA P2500S), which is then fed by a loudspeaker (Peerless TC6WD0104) to produce sound radiations. Sound pressures are recorded by 1/4-inch condenser microphones (GRAS 40PH) at designated positions, which are collected by dynamic signal acquisition board (NI PXI-4498) with LabVIEW program and postprocessed in the MATLAB package. The fabricated DSM experimentally demonstrates 98.2% absorptance at 260 Hz [see the symbols in Fig. 4(b)], which is of good consistence with that in numerical simulations. To this end, an ultrasparse DSM is experimentally realized.

D. DSMs with varied filling ratios

We emphasize that the perfect absorption mechanism is applicable to DSMs with varied filling ratios. As demonstrations, we here have optimized three DSMs with filling

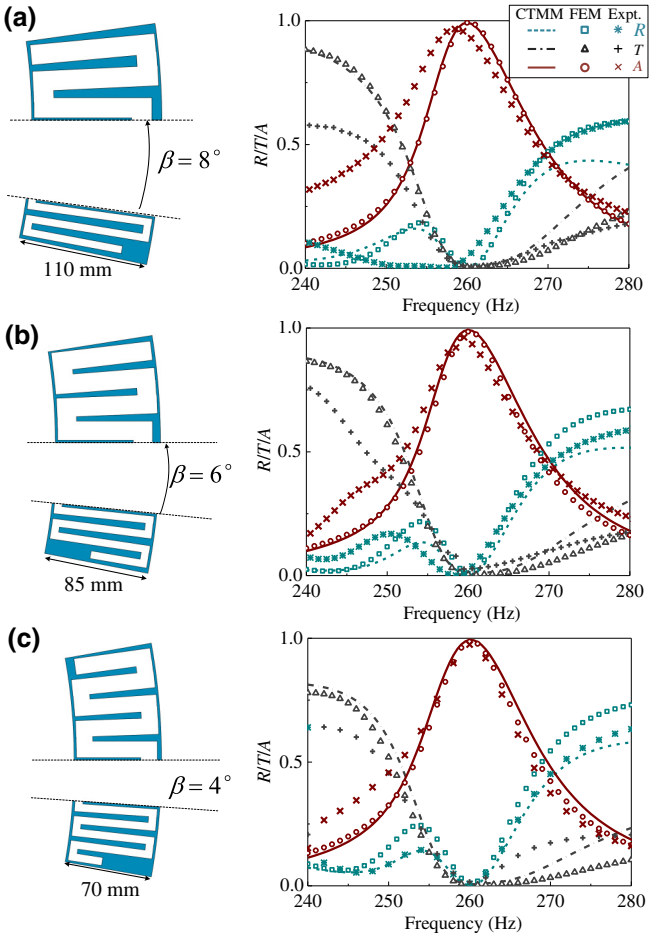

FIG. 5. Realizations of DSMs with varied filling ratios at (a) 40%, (b) 30%, and (c) 20%. The left and right panels are for 2D schematics and corresponding acoustical performances.

ratios of air channel at η=40 % ($\beta = 8°$), 30 % ($\beta = 6°$), and 20 % ($\beta = 4°$), as presented in Fig. 5. The left panels depict the 2D top view of metamolecules (marked as DSM1, DSM2, and DSM3, respectively) with corresponding geometrical parameters listed in Table II. The results show that perfect absorption is achieved at 260 Hz in all the three configurations. Although sparsity is decreased from DSM1 to DSM3, the structure goes deeper subwavelength as the corresponding thicknesses are 110 mm (1/12λ), 85 mm (1/15.5λ), and 70 mm (1/18.8λ), respectively.

TABLE II. Geometric parameters of FPRs (unit, mm).

	w_1	w_2	l_1	l_2	l_t	R_1	R_2
DSM1	6.8	17.8	319	326	89	498.5	608.5
DSM2	6.7	17.5	318.8	326	67.6	498.5	583.5
DSM3	6.4	15.7	319	326	54.5	498.5	568.5

E. Designing a broadband DSM

The diagram is further extended to design a broadband DSM. The inset of Fig. 6(b) depicts the 2D top view of the designed broadband DSM metamolecule, which is constituted by four FPRs. Here, the distances from FPR2 to FPR3 and FPR3 to FPR4 are defined as l_{t1} and l_{t2}, respectively; other parameters are named the same way as in Fig. 1. The fitness function is set as the sum of absorption coefficients at 260, 275, and 290 Hz. The optimized parameters [w_1, w_2, w_3, w_4, l_1, l_2, l_3, l_4, l_t, l_{t1}, l_{t2}] are obtained as [5.7, 5.7, 7.8, 17.7, 291, 305, 319, 326, 20, 50.2, 95.1] mm. Figure 6(a) presents the reflectance, transmittance, and absorptance of the optimized broadband DSM, which demonstrates that > 80% absorption can be achieved from 257 to 289 Hz. The minor deviation in spectra width may arise from multiple effects induced by the real lab measurement environments that differ from those of the simulation settings, including the fabrication error of sample, finite wall thickness of the channel, limited length of the sponge, and insufficient distance between the sample and sponge layer. As for the sound insulating performance, we here investigate the sound transmission loss (STL) given by $20\log_{10}|t_p|$, as presented in Fig. 6(b). It is demonstrated that approximately > 10 dB transmission loss (the average value in experiment is 13 dB) can be achieved at the frequency range. Moreover, the absorption bandwidth can be further extended by hybridizing more resonant atoms connected in a cascade manner (see Appendix B). The

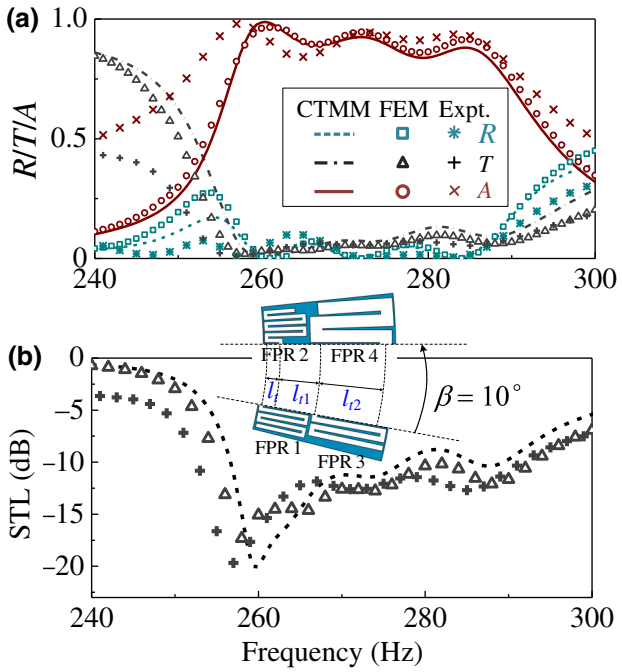

FIG. 6. (a) Acoustic spectra for a broadband DSM. (b) Sound transmission loss along with frequency. Inset: 2D view of the constructed broadband DSM.

broadband absorption and insulation characteristics may supply more possibilities in realistic applications.

IV. CONCLUSION

To conclude, an ultrasparse sound metacage that can completely consume sound radiations and allow airflow to circulate is established and optimized by introducing an inverse-design methodology. The perfect absorption originates from the effective coupling between a dissipated meta-atom and an acoustically soft boundary with their geometric parameters being optimized by GA. For experimental characterization, a measurement method conducted in a fan-shaped impedance tube is developed. The experimental results agree well with that derived by CTMM and FEM. Prototype DSMs showing varied filling ratio and broadband operation band are demonstrated to extend its practical scenario. Our proposal provides a perspective to develop ventilated absorbers for low-frequency sound.

ACKNOWLEDGMENTS

This work is supported by National Basic Research Program of China (2017YFA0303702), NSFC (Grants No. 12225408, No. 12074183, No. 11922407, No. 11834008, No. 11874215, and No. 12004176), Jiangsu Provincial NSF (BK20200298).

APPENDIX A: SPECTRA IN FINITE-ELEMENT METHOD

To derive the acoustic scattering spectra (including reflectance, transmittance, and absorptance) of an annular structure excited by a line source at its center, as presented in Fig. 7, it necessitates retrieving sound pressure in three radial positions. Here, sound pressures in circles with radii of r_1, r_2, and r_3 are retrieved. According to the rigorous scattering theory, sound pressures can be expressed as

$$p_1 = X_1 H_0^{(1)}(k_0 r_1) + Y_1 H_0^{(2)}(k_0 r_1), \tag{A1a}$$

$$p_2 = X_1 H_0^{(1)}(k_0 r_2) + Y_1 H_0^{(2)}(k_0 r_2), \tag{A1b}$$

$$p_3 = Y_2 H_0^{(2)}(k_0 r_3). \tag{A1c}$$

Here, the coefficients X_1, Y_1, and Y_2 can be determined

$$X_1 = \frac{H_0^{(2)}(k_0 r_2)p_1 - H_0^{(2)}(k_0 r_1)p_2}{H_0^{(1)}(k_0 r_1)H_0^{(2)}(k_0 r_2) - H_0^{(2)}(k_0 r_1)H_0^{(1)}(k_0 r_2)}, \tag{A2a}$$

$$Y_1 = \frac{H_0^{(1)}(k_0 r_1)p_2 - H_0^{(1)}(k_0 r_2)p_1}{H_0^{(1)}(k_0 r_1)H_0^{(2)}(k_0 r_2) - H_0^{(2)}(k_0 r_1)H_0^{(1)}(k_0 r_2)}, \tag{A2b}$$

$$Y_2 = \frac{p_3}{H_0^{(2)}(k_0 r_3)}. \tag{A2c}$$

Thus, we obtain the reflection and transmission coefficients of sound pressure

$$r_p = \frac{X_1}{Y_1} = \frac{H_0^{(2)}(k_0 r_2)p_1 - H_0^{(2)}(k_0 r_1)p_2}{H_0^{(1)}(k_0 r_1)p_2 - H_0^{(1)}(k_0 r_2)p_1}, \tag{A3a}$$

$$t_p = \frac{Y_2}{Y_1} = \frac{p_3}{H_0^{(2)}(k_0 r_3)} \times \frac{H_0^{(1)}(k_0 r_1)H_0^{(2)}(k_0 r_2) - H_0^{(2)}(k_0 r_1)H_0^{(1)}(k_0 r_2)}{H_0^{(1)}(k_0 r_1)p_2 - H_0^{(1)}(k_0 r_2)p_1}. \tag{A3b}$$

By substituting Eq. (A3) into Eqs. (6)–(8), the scattering spectra for sound energy can be derived.

APPENDIX B: EXTENDED BROADBAND ABSORPTION

It is predicable that absorption bandwidth can be further extended if more resonant atoms connected in a cascade way are hybridized. As a demonstration, we here design a broadband DSM by integrating six FPRs, as sketched in Fig. 8(a). The optimized parameters are listed as follows: the channel widths of the resonators $[w_1, w_2, w_3, w_4, w_5, w_6]$ = [5.6, 4.8, 5.4, 8.7, 8.7, 20] mm; the channel lengths $[l_1, l_2, l_3, l_4, l_5, l_6]$ = [262, 275, 290, 304.5, 319.2, 322] mm,

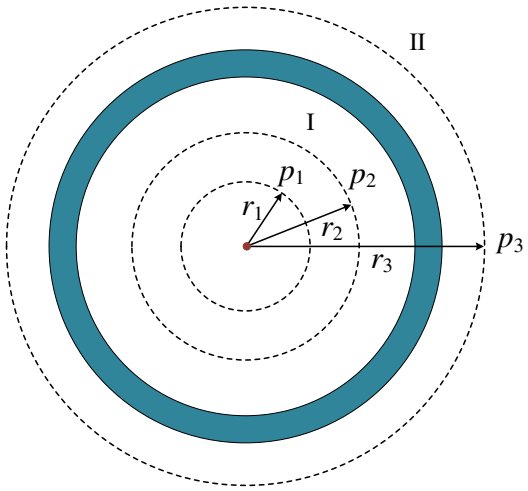

FIG. 7. 2D view of an annular structure excited by a line sound source located at its center. r_1, r_2, and r_3 are radii at which sound pressures are retrieved.

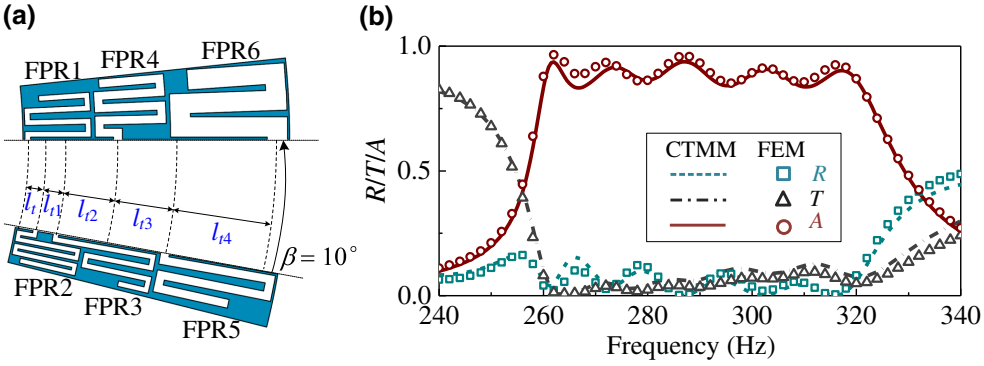

FIG. 8. (a) 2D view of the broadband DSM showing > 80% absorption ranging from 260 to 321 Hz. (b) Scattering spectra of the broadband DSM.

and the interval distances between resonators $[l_t, l_{t1}, l_{t2}, l_{t3}, l_{t4}]$ = [15.3, 18.5, 44.4, 61, 101] mm. The total thickness of the DSM in this case is 262 mm. Figure 8(b) presents the scattering spectra of the broadband DSM, where lines and symbols correspond to the results achieved by CTMM and FEM. It is demonstrated that > 80% absorption within frequency range from 260 to 321 Hz is achieved, which is wider than that achieved by four FPRs (see Fig. 6).

[1] B. Assouar, B. Liang, Y. Wu, Y. Li, J.-C. Cheng, and Y. Jing, Acoustic metasurfaces, Nat. Rev. Mater. **3**, 460 (2018).

[2] G. Ma and P. Sheng, Acoustic metamaterials: From local resonances to broad horizons, Sci. Adv. **2**, e1501595 (2016).

[3] N. Kaina, F. Lemoult, M. Fink, and G. Lerosey, Negative refractive index and acoustic superlens from multiple scattering in single negative metamaterials, Nature **525**, 77 (2015).

[4] M. Ambati, N. Fang, C. Sun, and X. Zhang, Surface resonant states and superlensing in acoustic metamaterials, Phys. Rev. B **75**, 195447 (2007).

[5] K. Melde, A. G. Mark, T. Qiu, and P. Fischer, Holograms for acoustics, Nature **537**, 518 (2016).

[6] A. Marzo and B. W. Drinkwater, Holographic acoustic tweezers, Proc. Nat. Acad. Sci. **116**, 84 (2019).

[7] S. A. Cummer and D. Schurig, One path to acoustic cloaking, New J. Phys. **9**, 45 (2007).

[8] A. N. Norris, Acoustic cloaking theory, Proc. R. Soc. A. **464**, 2411 (2008).

[9] B.-I. Popa, L. Zigoneanu, and S. A. Cummer, Experimental Acoustic Ground Cloak in Air, Phys. Rev. Lett. **106**, 253901 (2011).

[10] Z. Yang, F. Gao, X. Shi, X. Lin, Z. Gao, Y. Chong, and B. Zhang, Topological Acoustics, Phys. Rev. Lett. **114**, 114301 (2015).

[11] Z. Zhang, Q. Wei, Y. Cheng, T. Zhang, D. Wu, and X. Liu, Topological Creation of Acoustic Pseudospin Multipoles in a Flow-Free Symmetry-Broken Metamaterial lattice, Phys. Rev. Lett. **118**, 084303 (2017).

[12] G. Ma, M. Yang, S. Xiao, Z. Yang, and P. Sheng, Acoustic metasurface with hybrid resonances, Nat. Mater. **13**, 873 (2014).

[13] J. Mei, G. Ma, M. Yang, Z. Yang, W. Wen, and P. Sheng, Dark acoustic metamaterials as super absorbers for low-frequency sound, Nat. Commun. **3**, 756 (2012).

[14] V. Leroy, A. Strybulevych, M. Lanoy, F. Lemoult, A. Tourin, and J. H. Page, Superabsorption of acoustic waves with bubble metascreens, Phys. Rev. B **91**, 020301(R) (2015).

[15] X. Cai, Q. Guo, G. Hu, and J. Yang, Ultrathin low-frequency sound absorbing panels based on coplanar spiral tubes or coplanar Helmholtz resonators, Appl. Phys. Lett. **105**, 121901 (2014).

[16] Y. Li and B. M. Assouar, Acoustic metasurface-based perfect absorber with deep subwavelength thickness, Appl. Phys. Lett. **108**, 063502 (2016).

[17] J. Li, W. Wang, Y. Xie, B.-I. Popa, and S. A. Cummer, A sound absorbing metasurface with coupled resonators, Appl. Phys. Lett. **109**, 091908 (2016).

[18] N. Jiménez, V. Romero-García, V. Pagneux, and J.-P. Groby, Quasiperfect absorption by subwavelength acoustic panels in transmission using accumulation of resonances due to slow sound, Phys. Rev. B **95**, 014205 (2017).

[19] K. Donda, Y. Zhu, S.-W. Fan, L. Cao, Y. Li, and B. Assouar, Extreme low-frequency ultrathin acoustic absorbing metasurface, Appl. Phys. Lett. **115**, 173506 (2019).

[20] F. Wu, Y. Xiao, D. Yu, H. Zhao, Y. Wang, and J. Wen, Low-frequency sound absorption of hybrid absorber based on micro-perforated panel and coiled-up channels, Appl. Phys. Lett. **114**, 151901 (2019).

[21] A. Geslain, J.-P. Groby, V. Romero-García, F. Cervera, and J. Sánchez-Dehesa, Acoustic characterization of silica aerogel clamped plates for perfect absorption, J. Non-Cryst. Solids **499**, 283 (2018).

[22] M. Yang and P. Sheng, Sound absorption structures: From porous media to acoustic metamaterials, Annu. Rev. Mater. Res. **47**, 83 (2017).

[23] C. Zhang and X. Hu, Three-Dimensional Single-Port Labyrinthine Acoustic Metamaterial: Perfect Absorption with Large Bandwidth and Tunability, Phys. Rev. Appl. **6**, 064025 (2016).

[24] M. Yang, S. Chen, C. Fu, and P. Sheng, Optimal sound-absorbing structures, Mater. Horiz. **4**, 673 (2017).

[25] X. Peng, J. Ji, and Y. Jing, Composite honeycomb metasurface panel for broadband sound absorption, J. Acoust. Soc. Am. **144**, EL255 (2018).

[26] H. Long, C. Shao, C. Liu, Y. Cheng, and X. Liu, Broadband near-perfect absorption of low-frequency sound by subwavelength metasurface, Appl. Phys. Lett. **115**, 103503 (2019).

[27] Z. Zhou, S. Huang, D. Li, J. Zhu, and Y. Li, Broadband impedance modulation via non-local acoustic metamaterials, Natl. Sci. Rev. **9**, nwab171 (2021).

[28] Y. Zhu, A. Merkel, K. Donda, S. Fan, L. Cao, and B. Assouar, Nonlocal acoustic metasurface for ultrabroadband sound absorption, Phys. Rev. B **103**, 064102 (2021).

[29] A. Merkel, G. Theocharis, O. Richoux, V. Romero-García, and V. Pagneux, Control of acoustic absorption in one-dimensional scattering by resonant scatterers, Appl. Phys. Lett. **107**, 244102 (2015).

[30] H. Long, Y. Cheng, and X. Liu, Asymmetric absorber with multiband and broadband for low-frequency sound, Appl. Phys. Lett. **111**, 143502 (2017).

[31] N. Jiménez, V. Romero-García, V. Pagneux, and J.-P. Groby, Rainbow-trapping absorbers: Broadband, perfect and asymmetric sound absorption by subwavelength panels for transmission problems, Sci. Rep. **7**, 13595 (2017).

[32] T. Lee, T. Nomura, E. M. Dede, and H. Iizuka, Ultrasparse Acoustic Absorbers Enabling Fluid Flow and Visible-Light Controls, Phys. Rev. Appl. **11**, 024022 (2019).

[33] X. Wang, X. Luo, H. Zhao, and Z. Huang, Acoustic perfect absorption and broadband insulation achieved by double-zero metamaterials, Appl. Phys. Lett. **112**, 021901 (2018).

[34] L. Gu, C. Zhao, K. Wang, S. Li, X. Wang, and Z. Huang, Asymmetric sound absorption achieved by double-layer piezoelectric metamaterials with tunable shunt circuit, Appl. Phys. Lett. **119**, 131903 (2021).

[35] H. Long, C. Liu, C. Shao, Y. Cheng, J. Tao, X. Qiu, and X. Liu, Tunable and broadband asymmetric sound absorptions with coupling of acoustic bright and dark modes, J. Sound Vib. **479**, 115371 (2020).

[36] V. Romero-García, N. Jiménez, J.-P. Groby, A. Merkel, V. Tournat, G. Theocharis, O. Richoux, and V. Pagneux, Perfect Absorption in Mirror-Symmetric Acoustic Metascreens, Phys. Rev. Appl. **14**, 054055 (2020).

[37] H. Long, C. Shao, Y. Cheng, J. Tao, and X. Liu, High absorption asymmetry enabled by a deep-subwavelength ventilated sound absorber, Appl. Phys. Lett. **118**, 263502 (2021).

[38] C. Shen, Y. Xie, J. Li, S. A. Cummer, and Y. Jing, Acoustic metacages for sound shielding with steady air flow, J. Appl. Phys. **123**, 124501 (2018).

[39] C. Liu, J. Shi, W. Zhao, X. Zhou, C. Ma, R. Peng, M. Wang, Z. H. Hang, X. Liu, J. Christensen, N. X. Fang, and Y. Lai, Three-Dimensional Soundproof Acoustic Metacage, Phys. Rev. Lett. **127**, 084301 (2021).

[40] S. Molesky, Z. Lin, A. Y. Piggott, W. Jin, J. Vucković, and A. W. Rodriguez, Inverse design in nanophotonics, Nat. Photon. **12**, 659 (2018).

[41] N. Wang, W. Yan, Y. Qu, S. Ma, S. Z. Li, and M. Qiu, Intelligent designs in nanophotonics: From optimization towards inverse creation, PhotoniX **2**, 1 (2021).

[42] Y. Jin, L. He, Z. Wen, B. Mortazavi, H. Guo, D. Torrent, B. Djafari-Rouhani, T. Rabczuk, X. Zhuang, and Y. Li, Intelligent on-demand design of phononic metamaterials, Nanophotonics **11**, 439 (2022).

[43] D. Whitley, A genetic algorithm tutorial, Stat. Comput. **4**, 65 (1994).

[44] S. Katoch, S. S. Chauhan, and V. Kumar, A review on genetic algorithm: Past, present, and future, Multimedia Tools Appl. **80**, 8091 (2021).

[45] Z. Liu, X. Liu, Z. Xiao, C. Lu, H.-Q. Wang, Y. Wu, X. Hu, Y.-C. Liu, H. Zhang, and X. Zhang, Integrated nanophotonic wavelength router based on an intelligent algorithm, Optica **6**, 1367 (2019).

[46] L. Fan and J. Mei, Acoustic Metagrating Circulators: Nonreciprocal, Robust, and Tunable Manipulation with Unitary Efficiency, Phys. Rev. Appl. **15**, 064002 (2021).

[47] J. Li, A. Díaz-Rubio, C. Shen, Z. Jia, S. Tretyakov, and S. Cummer, Highly Efficient Generation of Angular Momentum with Cylindrical Bianisotropic Metasurfaces, Phys. Rev. Appl. **11**, 024016 (2019).

[48] M. M. Elsawy, S. Lanteri, R. Duvigneau, J. A. Fan, and P. Genevet, Numerical optimization methods for metasurfaces, Laser Photon. Rev. **14**, 1900445 (2020).

[49] R. E. Christiansen, F. Wang, and O. Sigmund, Topological Insulators by Topology Optimization, Phys. Rev. Lett. **122**, 234502 (2019).

[50] A. Y. Piggott, J. Lu, T. M. Babinec, K. G. Lagoudakis, J. Petykiewicz, and J. Vučković, Inverse design and implementation of a wavelength demultiplexing grating coupler, Sci. Rep. **4**, 7210 (2014).

[51] T. W. Hughes, M. Minkov, I. A. Williamson, and S. Fan, Adjoint method and inverse design for nonlinear nanophotonic devices, ACS Photonics **5**, 4781 (2018).

[52] P. R. Wiecha, A. Arbouet, C. Girard, and O. L. Muskens, Deep learning in nano-photonics: Inverse design and beyond, Photon. Res. **9**, B182 (2021).

[53] M. R. Stinson, The propagation of plane sound waves in narrow and wide circular tubes, and generalization to uniform tubes of arbitrary cross-sectional shape, J. Acoust. Soc. Am. **89**, 550 (1991).